GRC Transactions, Vol. 42, 2018

A Baseline Thermal Infrared Survey of Ground Heating Around the Casa Diablo Geothermal Plant, Mammoth Lakes, CA

R. Greg Vaughan[1], Deborah Bergfeld[2], William C. Evans[2], Stuart Wilkinson[2], Chris Miwa[3], and Mousa Diabat[3]

1- U.S. Geological Survey, Astrogeology Science Center, Flagstaff, AZ

2- U.S. Geological Survey, Volcano Science Center, Menlo Park, CA

3- Quantum Spatial, Inc., Corvallis, OR

Keywords

Airborne Thermal Infrared, Remote Sensing, Geothermal Site Characterization, Casa Diablo

ABSTRACT

In October 2016, an airborne thermal infrared (TIR) survey was conducted over the area surrounding the Casa Diablo geothermal power plant, near Mammoth Lakes, CA. This data collection campaign was part of an ongoing monitoring program to assess the potential impacts of geothermal energy production on the natural surface expression of the geothermal system. The purpose of the TIR survey was to characterize and map existing thermal ground in the study area, establishing a baseline against which any future changes may be compared.

The high spatial resolution (≤ 1-m pixel) imagery covers existing and proposed well fields, known geothermal areas, and part of the town of Mammoth Lakes. The TIR data were acquired at night, under clear skies and with snow-free ground, using a nadir-looking FLIR SC6000 sensor installed on a fixed-wing airplane, flown at an altitude of 1800 m above ground level. More than 3,400 overlapping image frames were acquired covering the 51-km^2 study area. Raw data values were converted to radiometric temperatures based on the radiometric calibration of the TIR sensor and compared to *in situ* surface temperature data collected concurrently within the study area. A temperature orthomosaic was created using Photoscan Pro image processing software.

Nine distinct thermal areas (including two previously unstudied sites) were mapped and characterized with the nighttime TIR imagery. Radiant background surface temperatures were below freezing at the time of the data collection. Pixel temperatures in the thermal areas ranged from 25 to 77 °C above the average temperature of ground surface. Estimates of the geothermal

radiant emittance of the thermal areas ranged from 10 to 72 W/m^2; and estimates of the geothermal radiative power output summed for all the thermal areas ranged from 3 to 8 MW.

This work shows the utility of high-resolution airborne TIR surveys for geothermal site characterization and establishes a workflow for data processing that could be automated in the future.

1. Introduction

The Casa Diablo geothermal power plant, near the town of Mammoth Lakes, California, taps into the Long Valley Caldera hydrothermal system on the southwest flank of the Resurgent Dome (Figure 1). Initial power production at Casa Diablo began in 1985 with a single 10 MWe binary plant. Two additional 15 MWe binary plants came online in 1990 increasing the total capacity to 40 MWe (Sorey et al., 1995).

The natural surface expression of the geothermal system includes numerous zones with increased heat and gas emissions, and sometimes vegetation-kill. Here, we define *thermal area* as a contiguous area that includes one or more thermal features (e.g., fumaroles), that is bounded by the spatial extent of hydrothermally altered ground, hydrothermal mineral deposits, geothermal gas emissions, heated ground, and/or associated lack of vegetation.

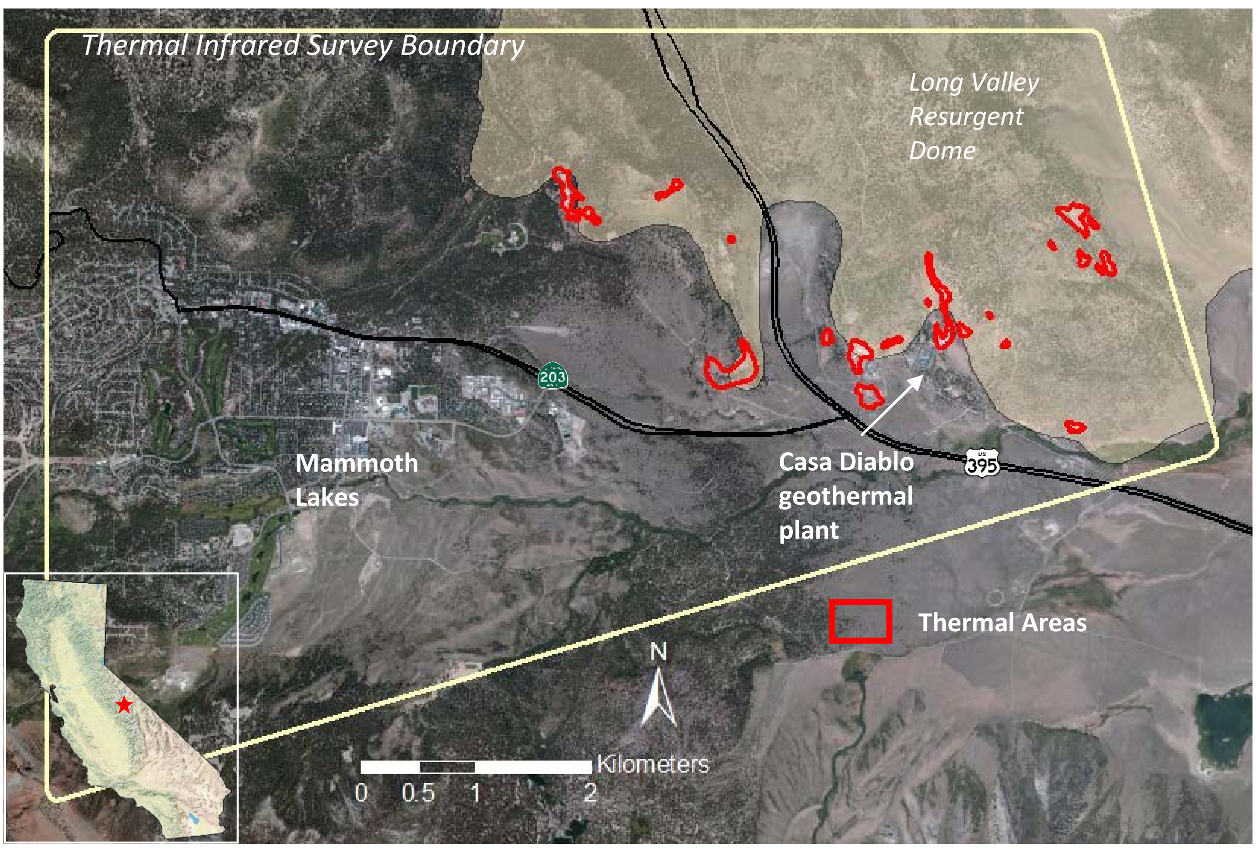

Figure 1. Location map of the study area, near Mammoth Lakes, CA, showing the Case Diablo geothermal plant, the town of Mammoth Lakes, the resurgent dome (light shading in the NE), and thermal areas identified by red borders.

Ground-based studies of soil temperature, soil-gas composition, and geothermal gas emission rates have been carried out over the past decades in these thermal areas (Sorey et al., 1998; Bergfeld et al., 2006; Bergfeld et al., 2011). These studies show that several of the thermal areas have increased in size during the 30-plus years of geothermal power production, although localized emission of gas and heat predated the onset of production at a few places (e.g., Basalt Canyon). Visual signs, like vegetation kills, often help to guide the ground-based studies. But given the large size of the area involved, field observations cannot assure that all thermally anomalous areas are found or fully constrained. Hence the need to employ a remote sensing technique like airborne thermal infrared (TIR) surveys. Nighttime TIR imagery of the study area was first collected in 2014. The results of that effort identified numerous known thermal areas, but showed the need for improved temperature calibration and geo-spatial correction (Bergfeld et al., 2015).

Since 2006 we've performed annual field surveys to measure diffuse CO_2 emissions and soil temperatures at the informally named Shady Rest thermal area about 3.2 km west of Casa Diablo (Figure 2). Our focus on Shady Rest relates to the direct response to new fluid production from 2 nearby geothermal wells that went on line in 2006. Initially we observed pockets of new vegetation kills that with time grew in size such that we needed to increase the size of the measurement grid. By 2011 the basic shape of the current grid which covers about 100,000 m^2 was in place, and as of 2017 new vegetation kills were contained within the bounds of the grid.

The diffuse CO_2 flux and shallow (20 cm) soil temperatures at the Shady Rest thermal area are positively correlated and maximum soil temperatures at measurement sites have been between 55-67 °C (131-152.6 °F) since 2011 (Bergfeld et al., 2015). There are several areas of steaming ground that have a more focused upflow of gas with temperatures as high as 92 °C (197.6 °F) – close to the boiling temperature of water at this elevation. Average CO_2 emissions over the thermal area are relatively uniform and total ~17 metric tonnes per day, ~6000 metric tonnes per year.

The 2016 TIR study was performed to establish baseline thermal metrics for monitoring and will help differentiate natural processes from human activities should any thermal areas increase in size or temperature or new thermal areas develop. Baseline thermal metrics include, spatial locations and areas of thermally emissive zones, surface temperatures, geothermal radiant emittance, and geothermal radiative power output.

2. Data

In October 2016, a high-resolution airborne TIR survey was conducted over the study area (Figure 1). Data were acquired at night (from 11:49 pm on October 10 to 2:23 am on October 11, 2016) from a fixed-wing Cessna Caravan aircraft, by contractor Quantum Spatial, Inc. A nadir-looking FLIR SC6000 sensor was installed and flown in the aircraft at an altitude of 1,800 m (5,905 ft) above ground level, which resolved a ground sampling distance (i.e. pixel size) of ≤1 m. The FLIR SC6000 camera measured radiance in a single broadband TIR channel ranging from 8.0-9.2 µm using a cooled quantum well infrared photodetector array, and had a noise equivalent temperature difference of 0.035 °C (0.063 °F). With a 50 mm focal length and 18° horizontal field of view, the 640x512 detector array covered a cross-track swath of ≤640 m (2,100 ft). Overlapping image frames were acquired along 24 parallel, opposing direction, overlapping flight lines, yielding 3,434 images covering the 51.24-km^2 (12,661-acre) study area.

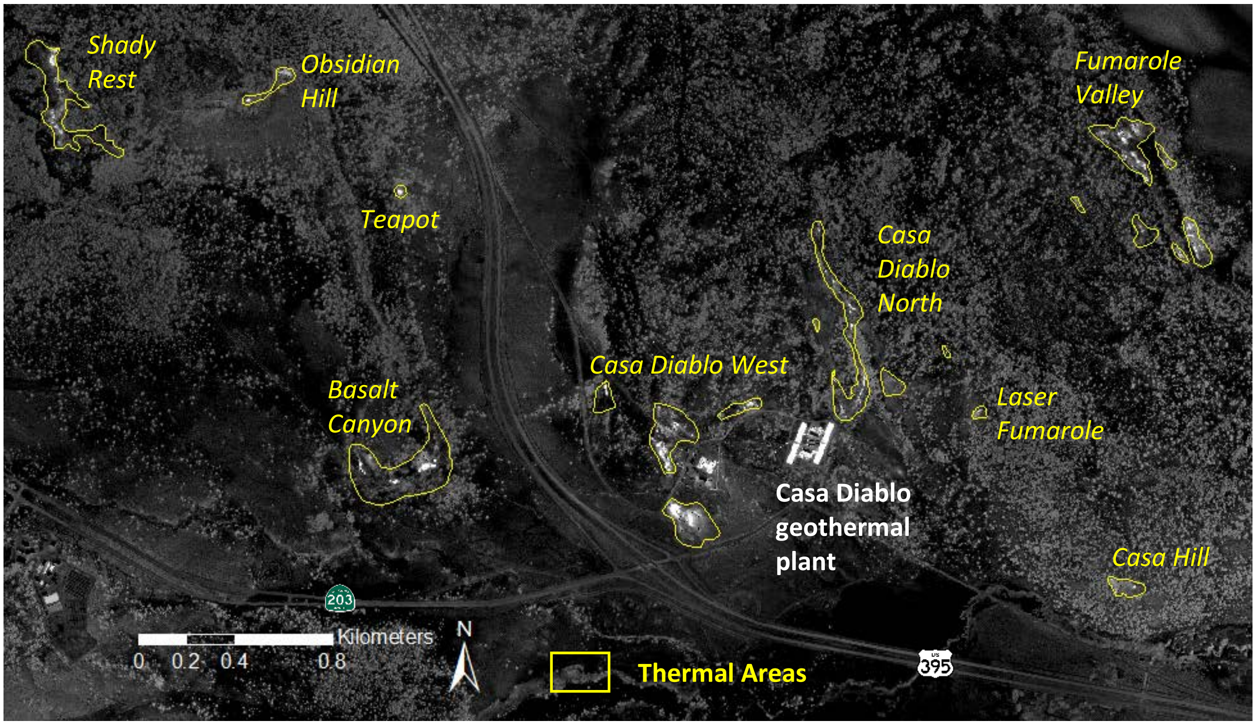

Figure 2. Thermal area map. The background is the thermal infrared mosaic of the study area. A linear contrast stretch is used to highlight thermal areas. Bright pixels are warmer.

During the data acquisition flight, the aircraft's position and attitude were measured by an onboard differential GPS and an inertial measurement unit. Two ground control monuments located within the survey area provided redundant control during the flight window and allowed for post-processing of the airborne GPS data. Several thermal targets (1m x 2m, highly TIR-reflective tarps) were placed in the field and their locations were surveyed to perform geospatial corrections to the photo block.

Calibrating the raw TIR data values to surface radiometric temperature occurred in two steps. Raw TIR data values were converted to radiometric temperatures (in °C) based on the FLIR factory-based radiometric calibration of the SC6000 TIR sensor and assuming a surface emissivity value of 0.96. Based on archives of laboratory-based spectral emissivity measurements of rocks and minerals, e.g., the Advanced Spaceborne Thermal Emission and Reflection Radiometer (ASTER) Spectral Library (speclib.jpl.nasa.gov; Baldridge et al., 2009), 0.96 is an appropriate TIR emissivity estimate for exposed rocks and soils. The radiometric temperatures were then adjusted based on concurrent atmospheric conditions (relative humidity and ambient air temperature) and *in situ* water temperature data. Atmospheric conditions were measured by a local meteorological station (Doe Ridge) – these data were publicly available. The ambient air temperature data from the Doe Ridge meteorological station were used to guide the temperature adjustment process, taking into account the attenuation of energy along the path between the surface and the sensor. Also, water temperatures were collected concurrently at 6 different sites within the study area using Onset HOBO ProV2™ temperature loggers equipped with two temperature sensors set to record data at 10-minute intervals. Water bodies make good calibration sites as they are usually large (relative to pixel size), stable, and thermally homogenous. The final product, a seamless TIR orthomosaic image of all overlapping frames, was created using the photogrammetric image processing software Photoscan Pro. The mosaic displays pixel temperature (in °C) accurate to within ~1 °C (1.8 °F), and with pixel geolocations accurate to within ~1 m.

3. Results and Interpretations

The temperatures in the final orthomosaic image ranged from about -20 to 75.2 °C (-4 to 167.4 °F). The lowest temperature values were almost always found over surfaces coated with high-TIR-reflectivity materials or metal surfaces, such as metal rooftops. Such surfaces appear cold because they reflect the down-welling TIR radiation emitted from the atmosphere. The sky's temperature is actually much colder than the lowest measurable temperature for this TIR sensor, -20 °C (-4 °F). Thus, retrieved temperatures over these metal surfaces did not necessarily represent their actual temperature. The hottest pixel in the orthomosaic, located at the Casa Diablo geothermal power plant, had a pixel temperature of 75.2 °C (167.4 °F). The upper measureable temperature limit for this sensor is around 650 °C (1202 °F), so there were no saturated pixels in the study area.

The ambient air temperature during the data acquisition overflights, which took place from 11:49 pm to 2:23 am, was about 8.5 °C (47.3 °F). Background surface temperatures were below freezing, ranging from -15 to -1 °C (5 to 30.2 °F). Barren ground, grassy fields, low shrub lands, and roads were below freezing at night. Thicker vegetation, like groups of tall trees, tends to hold in more heat over night and were slightly warmer, but still were often at, or just below, freezing. Table 1 shows a list of various surface features and materials and their typical radiometric pixel temperature ranges.

Table 1. Pixel temperature ranges for various surfaces in the orthomosaic image.

Metal roofs	-21 to -19 °C	-5.8 to -2.2 °F
Barren ground / Low dry grasses	-12 to -10 °C	10.4 to 14 °F
Grass on golf course / Baseball outfields	-15 to -14 °C	5 to 6.8 °F
Baseball infields (dirt)	-11 to -9 °C	12.2 to 15.8 °F
Shrublands	-9 to -5 °C	15.8 to 23 °F
Paved highway (395)	-7 to -1 °C	19.4 to 30.2 °F
Trees	-3 to 2 °C	26.6 to 33.8 °F
Pools / Hot tubs (in Mammoth Lakes)	7 to 35 °C	44.6 to 95 °F
Thermal Areas (including power plant)	3 to 75 °C	37.4 to 167 °F

3.1 Thermal Areas

Nine spatially distinct thermal areas were identified and mapped (Figure 2; Table 2). The Casa Diablo West and Casa Diablo North thermal areas are located adjacent to the power plant site. Mapping of the natural thermal areas here excludes warm features on engineered structures, such as wellheads, pipelines, heat exchangers, and cooling vents that are associated with geothermal energy production.

For each thermal area, a nearby non-thermal background area was defined. Background areas were characterized by proximity to thermal areas, sharing similar topography and elevation, and having similar surface cover, e.g., generally barren of vegetation (Vaughan et al., 2012; Vaughan et al., 2014). Then, for each thermal area, pixel temperature values were extracted, for pixels in the mapped thermal area that were >0, >1, >2, >3, and >4 standard deviations (σ) above the mean temperature value of the corresponding background area. The total radiant emittance (M_T, in W/m^2) from each thermal area, and each background area, was derived on a pixel-by-pixel basis using the Stephan-Boltzmann equation ($M_T = \sigma\varepsilon T^4$), where $\sigma = 5.6704*10^{-8}$ (W*m^{-2}*K^{-4}) and T = the retrieved radiometric pixel temperature (K). Emissivity (ε) for each area was derived from the North American ASTER Land Surface Emissivity Database, which is a seamless database of moderate-resolution (100-m pixels) land surface emissivity for North America derived from standard ASTER emissivity products, developed by Hulley and Hook (2009). The geothermal component of the radiant emittance (M_G) was calculated by subtracting the background radiant emittance (M_{BG}) from the total radiant emittance (M_T). The background subtraction technique minimizes the effects of seasonal variations in surface radiance and permits meaningful data intercomparison. The geothermal radiative power output (Φ_G, in kW) was attained by multiplying M_G by the corresponding pixel area (1x1-m pixels), and summed for all the pixels in the thermal area. These calculations were made for each thermal area – for all the pixels that were >0, >1, >2, >3, and >4 σ above the mean temperature of the background area. This generates a map showing the spatial extent of thermal areas as well as the distribution of heat within the thermals areas (Figures 3 and 4).

Table 2. Thermal area characteristics. T_{max} = maximum retrieved pixel temperature; $M_{G(2\sigma)}$ = Geothermal Radiant Emittance at the 2σ level; $\Phi_{G(2\sigma)}$ = Geothermal Radiative Power output at the 2σ level.

	Thermal Area	**T_{max}**	**$M_{G(2\sigma)}$ (W/m^2)**	**$\Phi_{G(2\sigma)}$ (kW)**
1	Shady Rest	19.6 °C (67.3 °F)	38.68	569
2	Teapot	17.4 °C (63.3 °F)	37.85	65
3	Obsidian Hill	18 °C (64.4 °F)	25.14	179
4	Basalt Canyon	43.3 °C (109.9 °F)	33.16	1136
5	Casa Diablo West	68.3 °C (154.9 °F)	46.33	2414
6	Casa Diablo North	50.5 °C (122.9 °F)	30.72	815
7	Laser Fumarole	24.4 °C (75.9 °F)	34.40	51
8	Casa Hill	23.1 °C (73.6 °F)	26.61	68
9	Fumarole Valley	26.9 °C (80.4 °F)	37.59	919

Around the thermal areas, the retrieved pixel temperatures of the background barren ground, low grass, and shrubs between the trees ranges from about -16 to -8 °C (3.2 to 17.6 °F); and the retrieved pixel temperatures of trees typically ranges from -2.5 to 2.5 °C (27.5 to 36.5 °F). Pixels with retrieved temperatures that are 1.5 to 2.5 °C (2.7 to 4.5 °F) above the local background temperature stand out as thermally emissive and are interpreted as geothermal. With respect to interpretation, it is important to recognize that there are some groves of trees that are as warm as some of the thermally emissive thermal areas. The key to differentiating between geothermal emission and warm materials that are not geothermal in origin is the high-spatial fidelity of the data. With 1-m pixels, combined with the high-precision geolocation of the pixels, individual trees can be identified and directly compared to high-resolution color orthoimagery for confirmation of interpretation. Exposed rocks on sun-facing slopes that are still warm at night are more difficult to differentiate from geothermally emissive areas.

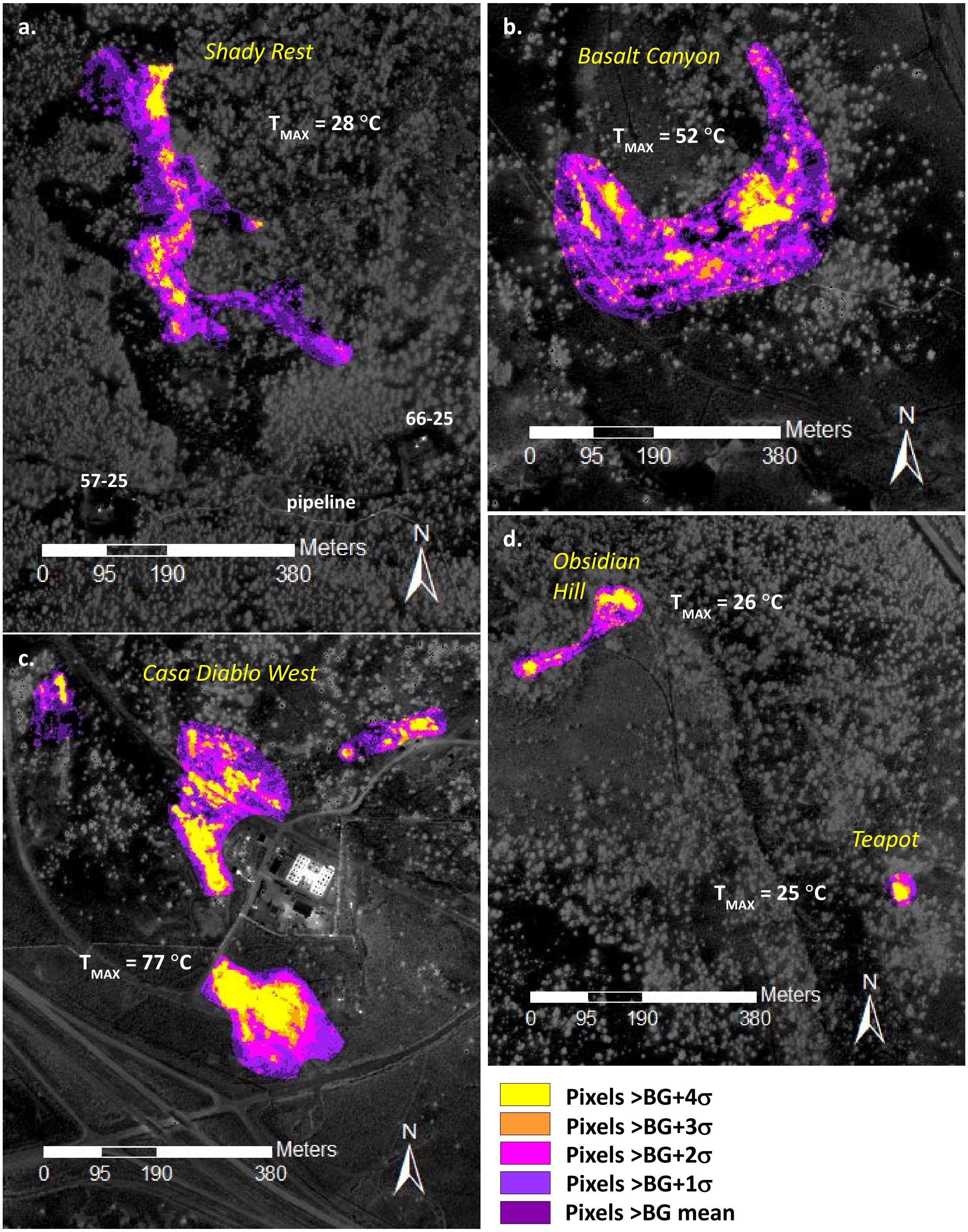

Figure 3. Thermal anomaly maps for selected thermal areas: (a) Shady Rest, including geothermal well heads and pipeline; (b) Basalt Canyon; (c) Casa Diablo West; (d) Obsidian Hill and Teapot. Colors represent pixels that are warmer than the local background in increments of 1, 2, 3, and 4 σ above the mean background temperature. T_{max} = maximum above-background temperature. The background image is the TIR mosaic.

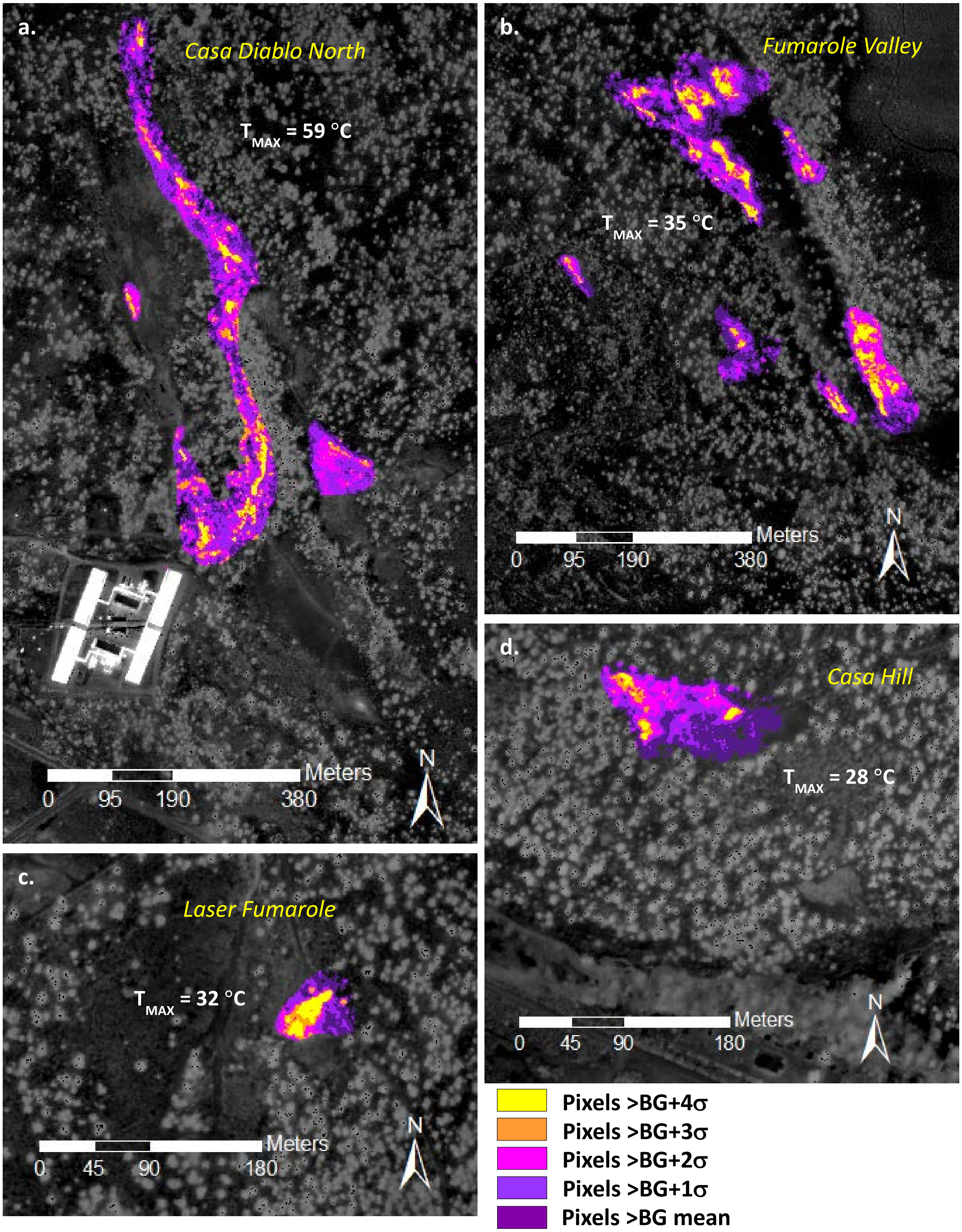

Figure 4. Thermal anomaly maps for selected thermal areas: (a) Casa Diablo North; (b) fumarole Valley; (c) Laser Fumarole; (d) Casa Hill. Colors represent pixels that are warmer than the local background in increments of 1, 2, 3, and 4 σ above the mean background temperature. T_{max} = maximum above-background temperature. The background image is the TIR mosaic.

3.2 Geothermal Infrastructure

Wellheads 57-25 and 66-25, near the Shady Rest thermal area were warm, 25.2 and 23.7 °C (77.4 and 74.7 °F), respectively, as was the pipeline that leads from these wells to the geothermal power plant (Figures 3a, 5a). Though the pixel temperatures of the pipeline were below 0 °C (32 °F), they were elevated 2 to 4 °C (3.6 to 7.2 °F) above the background, making the pipeline clearly visible in the TIR imagery. There were also notable hot spots along the pipeline, 4 to 17 °C (7.2 to 30.6 °F) above the mean pipeline temperature, which may indicate the locations of pipe joints or junctions, or possible thermal leaks (poor insulation). A temperature profile along the length of the pipeline (Figure 5b) shows about a dozen points where the pipeline temperature spikes several °C above the average, although the mean temperature remains remarkably

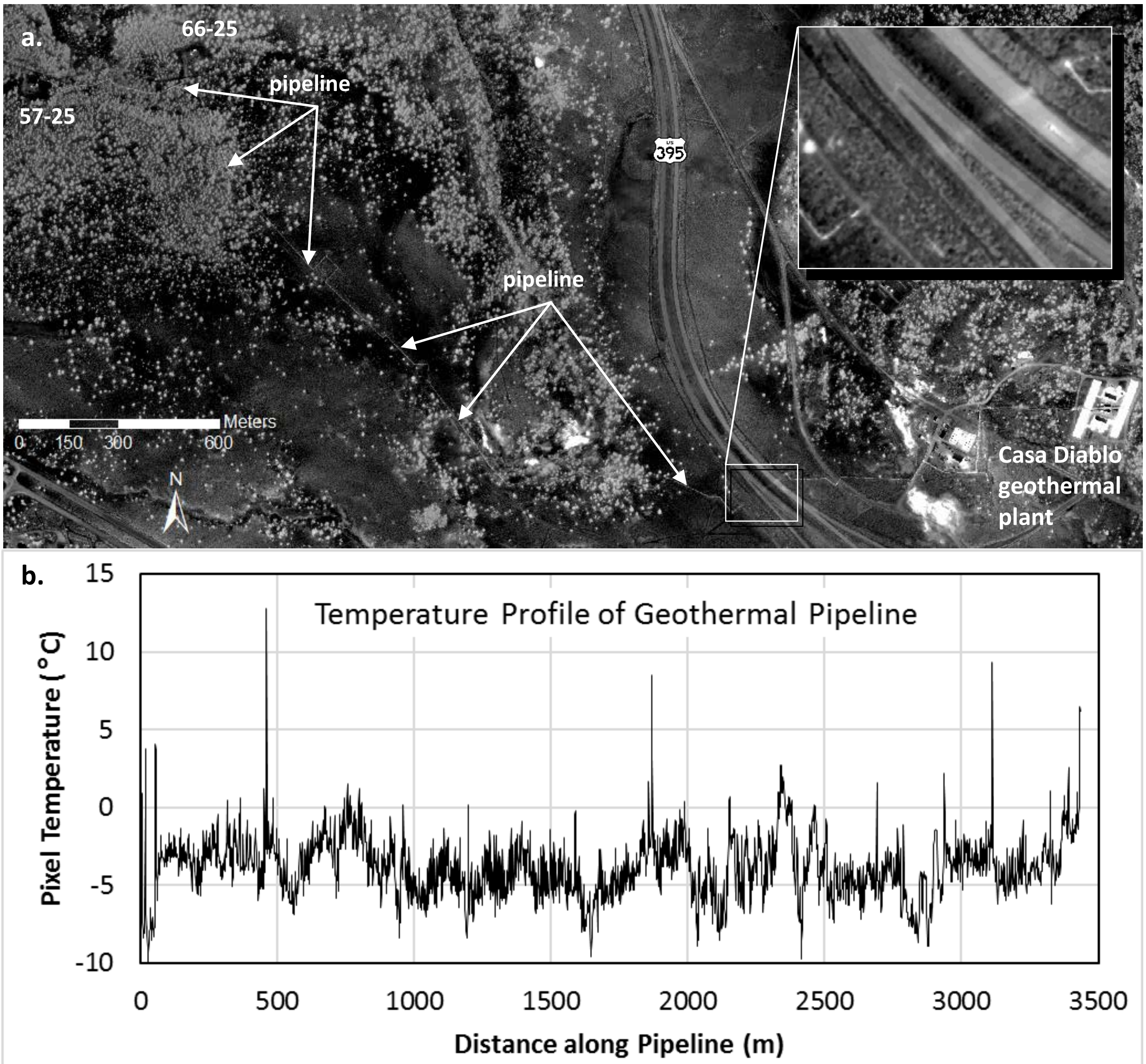

Figure 5. (a) Map highlighting the geothermal pipeline. Inset image: 1-2 °C thermal anomaly where pipeline goes under highway 395. (b) Temperature profile along 3.5-km pipeline, from well 57-25 to power plant.

consistent, losing less than 1 °C (1.8 °F), along its ~3.5 km length. The inset image in Figure 5a shows a detectable thermal anomaly of 1-2 °C (1.8-3.6 °F) on the surface of highway 395 above the location where the geothermal pipeline goes under the road.

The warmest pixels in the temperature orthomosaic, 50-75 °C (122 to 167 °F), are located at the geothermal power plant, spatially coincident with power plant structures, such as pipes, condensers, generators, and the cooling towers (Figure 6). Again the high spatial fidelity of the data allows an assessment of the structures, or parts of structures, that are radiating the most heat. For example, there is a cooling fan that is about 10 °C (18 ° F) warmer than the other fans.

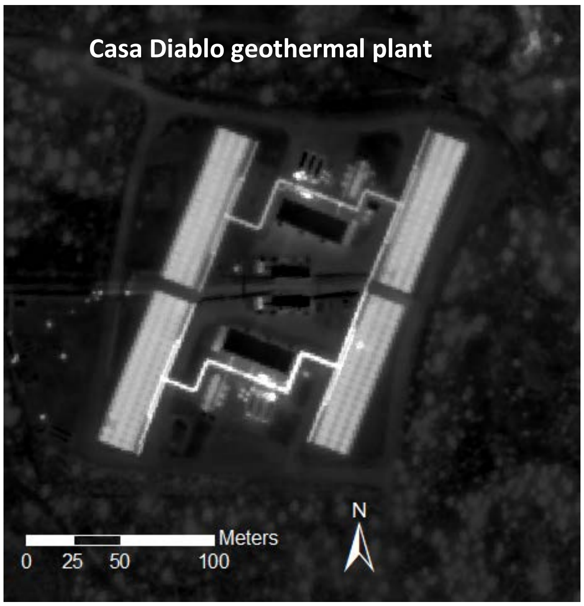

Figure 6. Temperature image of the Casa Diablo geothermal power plant, showing temperature distribution among the power plant structures, including a cooling fan that is about 10 °C (18 ° F) warmer than the other fans.

4. Discussion

4.1 Temperature Data Intercomparison

The process of properly geo-correcting / geo-locating and combining all the images into a temperature orthomosaic necessarily involves some pixel resampling. Multiple overlapping image frames were stitched together using software that automatically finds matching points among the temperature image frames and generates a point cloud for creating an orthomosaic. How does this process affect the precision of pixel temperature retrievals? To address this question, pixel temperature values for numerous sites in the orthomosaic were compared to pixel temperature values from the individual raw (un-resampled) temperature image frames. Twelve sites from different locations across the study area were selected for this intercomparison, with features ranging in temperature from -8 to 75 °C (17.6 to 167 °F). All of the selected features were covered by 2 overlapping, parallel, opposing direction flight lines. And because of the overlap in the along-track direction between successive image frames within a flight line, each feature was covered multiple times per flight line. For example, the warmest group of pixels in the Shady Rest thermal area was covered by 10 overlapping frames along one flight line, and by 6 overlapping frames along an adjacent flight line. Therefore, including the final temperature orthomosaic image, there are 17 temperature values retrieved for this group of pixels – and they are not all exactly the same in pixel-to-pixel terms.

There are two different intercomparisons to make. First, how well do pixel temperatures agree among the multiple overlapping image frames that have not been resampled and incorporated into the larger orthomosaic? In general, there was very good pixel temperature agreement among the individual images, from frame-to-frame, and from flight-line-to-flight-line (Figure 7a). For most sites analyzed, the retrieved pixel temperatures of any given feature varied less than 2 °C (3.6 °F). But there were some exceptions that are worth attention. For example, a fumarole in the Casa Diablo West thermal area (Fumarole 1 in Figure 7b), showed a pixel temperature range from 68 to 61 °C (154 to 141.8 °F) along a single flight path. In addition, this same fumarole averaged 63 °C (145.4 °F) in one flight line and 74 °C (165.2 °F) in the adjacent flight line – an 11 °C (20 °F) temperature difference. There were also examples of variations in retrieved pixel temperatures over human-made structures. For example, wellhead 57-25, as well as the scene's hottest pixel (located over some pipes at the geothermal power plant), showed pixel temperature variations ranging from 4 to 15 °C (39.2 to 59 °F) for the same feature, along the same flight line or between flight lines (Figure 7b). Such discrepancies could be explained by steam interference that varies with viewing geometry. Water droplets condensing as steam in the viewing path result in radiometric temperature measurements that represent the temperature of the steam, which interferes with temperature retrieval of the surface thermal feature beneath. In general, any thermal feature that is steaming during TIR data acquisition, could display pixel temperatures that vary by tens of °C due to the interference of steam that varies with time and with look angle. Another source of uncertainty in remote surface temperature retrievals is sub-pixel-scale thermal mixing, which also varies with viewing geometry. While the study area was surveyed at a relatively high spatial resolution of 1 meter, TIR pixels covered features with extreme temperature gradients. Temperatures retrieved for a pixel represent an average of all sub-pixel-scale radiating components, including the radiant temperature of the cooler background. Also, as the aircraft moved along its flight path, variations in viewing geometry can result in a single feature being represented by differently oriented pixels in different image frames.

The second intercomparison: how well do pixel temperatures from the unresampled, individual overlapping image frames agree with pixel temperatures from the orthomosaic? Here, there seems to be a small systematic bias (see Figure 7c). For natural surfaces, retrieved pixel temperatures in the orthomosaic are always lower than pixel temperatures in the individual frames, by an average of 1.9 °C (3.4 °F), and by as much as 3.2 °C (5.8 °F). Over the human-made structures analyzed, the bias is larger – pixel temperatures in the orthomosaic are 4.5 to 8.3 °C (8.1 to 14.9 °F) lower than the highest temperatures for the same features in the individual image frames. The most extreme example is that of some pipes near the power plant, which have the warmest pixels in the orthomosaic. The maximum retrieved pixel temperature in the unresampled temperature image frames for the warmest pixel (next to the geothermal power plant) is 83.5 °C (182.3 °F). This same spot is 75.2 °C (167.4 °F) in the orthomosaic. For such narrow, long geometry features with extreme temperature gradients, the final mosaicked orthoimagery can potentially contain a smoothing of the highest values when pixel locations are resampled during the mosaicking process. The smoothing procedure may have an opposite impact if trying to characterize cold-spots. Resampling techniques such as the 'nearest neighbor' method should be used when possible to best preserve the integrity of the original calibrated temperature value.

5. Conclusions

High-spatial resolution (~1-m pixels) TIR imaging surveys are extremely useful for mapping, characterizing, and monitoring geothermal sites. Nighttime, or pre-dawn, cloud-free sky, and snow-free surface data acquisition are critical conditions for minimizing the effects of solar irradiance and maximizing thermal contrast, particularly when studying surface thermal features that are sub-boiling in temperature.

The 2016 airborne TIR survey performed by Quantum Spatial, Inc. establishes a solid baseline against which any future changes to the surface expression the geothermal system may be compared. Changes in the surface expression of geothermal systems like this can be characterized by either changes in surface temperature, or changes in the exposed area of static high-temperatures. Measuring, for example, only the temperature statistics of a given area may not reveal all of the thermal changes that a thermal area could express. Thus, it is important to acquire well-calibrated TIR imagery that can be used to quantitatively estimate additional thermal metrics, such as geothermal radiant emittance and geothermal radiative power output.

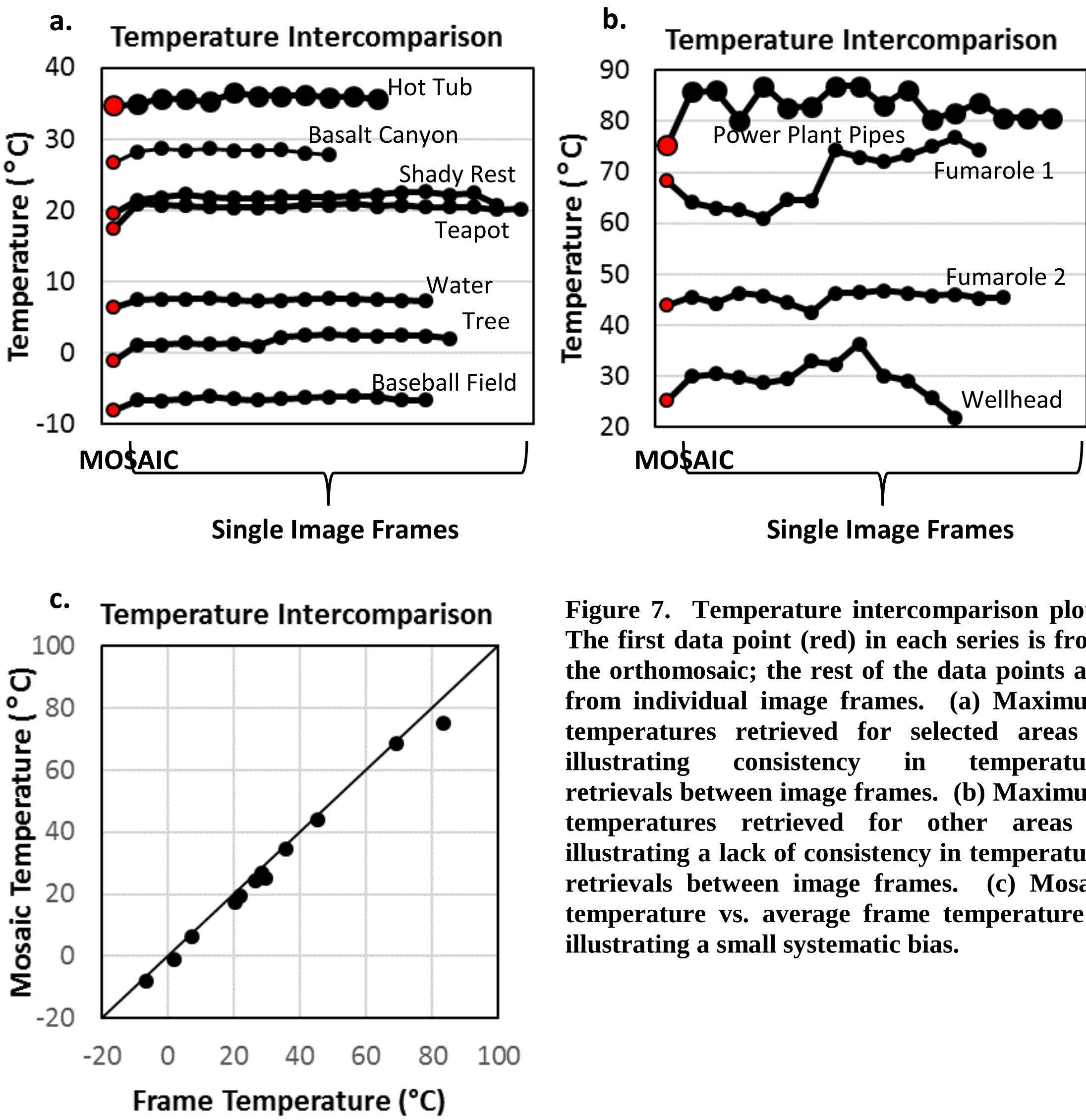

Figure 7. Temperature intercomparison plots. The first data point (red) in each series is from the orthomosaic; the rest of the data points are from individual image frames. (a) Maximum temperatures retrieved for selected areas – illustrating consistency in temperature retrievals between image frames. (b) Maximum temperatures retrieved for other areas – illustrating a lack of consistency in temperature retrievals between image frames. (c) Mosaic temperature vs. average frame temperature – illustrating a small systematic bias.

Table 3. Retrieved pixel temperatures for intercomparison sites.

Site	**T_{max} °C (frame)**	**T_{max} °C (mosaic)**	**ΔT °C**	**T_{max} °F (frame)**	**T_{max} °F (mosaic)**	**ΔT °F**
Warmest Pixel	83.5	75.2	8.3	182.3	167.4	14.9
Casa Diablo Fumarole 1	69.1	68.3	0.8	156.4	154.9	1.5
Casa Diablo Fumarole 2	45.5	43.8	1.7	113.9	110.8	3.0
Wellhead 57-25	29.7	25.2	4.5	85.4	77.4	8.1
Teapot Hottest Pixel	20.6	17.4	3.2	69.0	63.3	5.7
Shady Rest Hottest Pixel	22.0	19.6	2.4	71.5	67.3	4.2
Basalt Canyon Hottest Pixel	28.4	26.6	1.8	83.0	79.9	3.2
Water Treatment Pond	7.5	6.4	1.1	45.5	43.5	2.0
Shady Rest Baseball Infield	-6.4	-8.0	1.6	20.5	17.6	2.9
Village Lodge Hot Tub	35.8	34.6	1.2	96.4	94.3	2.1
Isolated Tree	1.9	-1.1	3.0	35.4	30.0	5.4
Laser Fumarole	26.5	24.4	2.1	79.8	75.9	3.9

Remotely derived surface temperatures are always underestimates of the actual surface temperature for several reasons, including sub-pixel thermal mixing and variable steam interference. Therefore, when combining multiple views of a single feature into an image mosaic, the maximum observed temperature should be used, rather than averaging temperature values.

The emissions of geothermal heat and gases are almost always inextricably linked. There are a few examples of cold degassing portions of some thermal areas that are not expressed by elevated surface temperatures, but such areas are rare in this study area. Measurements of both gases and geothermal heat output should be coupled, and field-based monitoring of soil temperature, soil-gas composition, and gas emission should be continued on a regular basis. Also, future TIR surveys of this area may be warranted should significant surface changes be observed. To achieve higher spatial resolution, if needed, future TIR surveys could employ an aircraft flown at a lower altitude or use unoccupied aerial systems (UAS) equipped with comparable TIR sensors. UAS surveys are often limited by the size of an area that can be covered in a single data acquisition campaign, and by the weight they can carry. But now that a good thermal baseline has been established, with good thermal areas maps, a UAS-based TIR survey that focuses on smaller areas could be done at lower cost and with higher frequency. Finally, this work lays out a framework for the possibility of automating a data processing and analysis workflow that could improve the efficiency of similar future studies.

6. Acknowledgements

Funding for this study was provided, in part, by the Bureau of Land Management, Bishop, California. Any use of trade, firm, or product names is for descriptive purposes only and does not imply endorsement by the U.S. Government.

REFERENCES

Baldridge, A.M., Hook, S.J., Grove, C.I., and Rivera, G., 2009. The ASTER spectral library version 2.0. Remote Sensing of Environment, 113(4), pp.711-715.

Bergfeld, D., Evans, W.C., Howle, J.F., Farrar C.D., 2006, Carbon dioxide emissions from vegetation-kill zones around the resurgent dome of Long Valley Caldera, eastern California, USA: Journal of Volcanology and Geothermal Research, v. 152, no. 1-2, p. 140–156.

Bergfeld, D., and W.C. Evans, 2011. Monitoring CO2 emissions in tree kill areas near the resurgent dome at Long Valley caldera, California: U.S. Geological Survey Scientific Investigations Report 2011-5038, 22 p.

Bergfeld, D., Vaughan, R.G., Evans, W.C. and Olsen, E., 2015. Monitoring Ground-Surface Heating During Expansion of the Casa Diablo Production Well Field at Mammoth Lakes, California. In GRC Annual Meeting & GEA Geothermal Energy Expo (Vol. 39, pp. 1007-1013).

Evans W.C., T.D. Lorenson, M.L. Sorey, and D. Bergfeld, 2004. Transport of injected isobutane by thermal groundwater in Long Valley caldera, California, USA. In Wanty RB, Seal II RR, editors. Water-Rock Interaction-11 2004; p. 125-129.

Hulley, G.C., and Hook, S.J., 2009, The North American ASTER land surface emissivity database (NAALSED) Version 2.0: Remote Sensing of Environment, v. 113, v. 9, p. 1967–1975.

Sorey, M.L., G.A. Suemnicht, N.C. Sturchio, and G.A. Nordquist, 1991. New evidence on the hydrothermal system in Long Valley caldera, California, from wells, fluid sampling, electrical geophysics, and age determinations of hot-spring deposits. J. Volcanol. Geotherm. Res., 48, 229–263.

Sorey, M.L., C.D. Farrar, G.A. Marshall, and J.F. Howle, 1995. Effects of geothermal development on deformation in the Long Valley caldera, eastern, California. J. Geophys. Res. 100, B7, 12475-12486.

Sorey, M.L., W.C. Evans, B.M. Kennedy, C.D. Farrar, L.J. Hainsworth, and B. Hausback, 1998. Carbon dioxide and helium emissions from a reservoir of magmatic gas beneath Mammoth Mountain, California J. Geophys. Res., 103, B7, 15,303-15,323.

Suemnicht, G.A., M.L. Sorey, J.N. Moore, and R. Sullivan, 2007. The shallow hydrothermal system of Long Valley caldera, California. In: Proceedings. Stanford, California, Thirty-Second Workshop on Geothermal Reservoir Engineering; 01/22/2007; Stanford, California. San Diego, CA: Stanford University; p. 465-470.

Sorey, M. L., McConnell, V. S., & Roeloffs, E. (2003). Summary of recent research in Long Valley caldera, California. Journal of volcanology and geothermal research, 127(3), 165-173.

Vaughan, R.G., Keszthelyi, L.P., Lowenstern, J.B., Jaworowski, C., and Heasler, H., 2012, Use of ASTER and MODIS thermal infrared data to quantify heat flow and hydrothermal change at Yellowstone National Park: Journal of Volcanology and Geothermal Research, v. 233–234, p. 72–89.

Vaughan, R.G., Heasler, H., Jaworowski, C., Lowenstern, J.B. and Keszthelyi, L.P., 2014. Provisional maps of thermal areas in Yellowstone National Park, based on satellite thermal infrared imaging and field observations (No. 2014-5137). US Geological Survey.